

# The spatial-temporal total friction coefficient of the fault viewed from the seismo-electromagnetic theory.

Patricio Venegas-Aravena (1, 2), Enrique G. Cordaro (2, 3), David Laroze (4).

(1) Department of Structural and Geotechnical Engineering, School of Engineering, Pontificia Universidad Católica de Chile, Vicuña Mackenna 4860, Macul, Santiago, Chile.

(2) Cosmic Radiation Observatories, University of Chile, Casilla 487-3, Santiago, Chile

(3) Facultad de Ingeniería, Universidad Autónoma de Chile, Pedro de Valdivia 425, Santiago, Chile.

(4) Instituto de Alta Investigación, CEDENNA, Universidad de Tarapacá, Casilla 7D, Arica, Chile.

Author: P. Venegas-Aravena: [plvenegas@uc.cl](mailto:plvenegas@uc.cl)

Co-author: E. G. Cordaro: [ecordaro@dfi.uchile.cl](mailto:ecordaro@dfi.uchile.cl)

Co-author: D. Laroze: [dlarozen@uta.cl](mailto:dlarozen@uta.cl)

## Abstract

Recently, it has been shown theoretically how the lithospheric stress changes could be linked with magnetic anomalies, frequencies, spatial distribution and the magnetic-moment magnitude relation using the electrification of microfractures in the semi brittle-plastic rock regimen [Venegas-Aravena *et al.* Nat. Hazards Earth Syst. Sci. **19**, 1639 – 1651 (2019)]. However, this Seismo-electromagnetic Theory still has not shown any relation, approach or changes in the fault's properties in order to be linked with the beginning of seismic rupture process itself. In this work we show the first and simple theoretical approach to one of the key parameters for seismic ruptures as is the friction coefficient and the stress drop. We use sigmoidal stress changes in the non-elastic regimen within lithosphere described before to figure out the temporal changes in frictional properties of faults. We also use a long term friction coefficient approximation that can depend on the fault dip angle, four parameters that weight the first and second stress derivative, the spatial distribution of the non-constant stress changes and the stress drop. It is found that the friction coefficient is not constant in time and evolve previous and after the earthquake occurs regardless of the (non-zero) weight used. When we use a dip angle close to 30 degrees and the contribution of the second derivative is more significant than the first derivative, the friction coefficient increase ~~previous~~ the earthquake. Then, the earthquake occurs and the friction drop. Finally, the friction coefficient increases and decreases after the earthquake. When there is no contribution of stress changes in the semi brittle-plastic regimen, no changes are expected in the friction coefficient.

Keywords: Seismo-electromagnetic Theory, Friction coefficient, Magnetism, Earthquakes, LAIC effect.

## 1.- Introduction

~~During recent years, several works have appeared in different magnetic and ionospheric measurements that seem related to earthquakes. These measurements are part of the lithosphere-atmosphere-ionosphere-coupling effect (or LAIC effect) (e.g. De Santis et al., 2019a). Some researchers have shown co-seismic magnetic variations during some earthquakes (e.g. Utada et al. (2011) during Tohoku 2011 earthquake). Others researches have been focus on the oscillation frequency ( $\mu\text{Hz} - \text{kHz}$  range) of magnetic field previous the occurrence of some earthquakes (Schekotov and Hayakawa, 2015; Cordaro et al., 2018; Potirakis et al., 2018a, b, among other). The magnetic anomalies have also been widely studied. For instance, De Santis et al. (2019b) have recently found an increase in the amount of daily magnetic~~

1 ~~anomalies previous 12 earthquakes between 2014 and 2016. This increase also was found by other~~  
2 ~~researchers (e.g. Marchetti and Akhoondzadeh (2018)).~~

3

4 On the other hand, experiments using rocks samples ~~suffering~~ fast changes on the uniaxial stress ~~create~~  
5 microfractures, the displacement of dislocations and electrification in the semi brittle-plastic rock regimen  
6 (e.g. Anastasiadis et al., 2004). This physical mechanism of rock electrification is described  
7 mathematically by The Motion of Charged Edge Dislocations (MCD) model (e.g. see Vallianatos and  
8 Tzanis (1998) or Vallianatos and Tzanis (2003) for a comprehensive derivation of MCD model). This  
9 model seems to be a plausible electromechanical mechanism that could explain the magnetic  
10 measurements. Because of that Venegas-Aravena et al. (2019) developed a Seismo-electromagnetic  
11 Theory based on experimental microcracks and stress changes. This theory showed how the fractal nature  
12 of the cracks could explain the magnetic frequency range, the co-seismic magnetic field and the conditions  
13 for generating magnetic anomalies. However, this theory (in addition to others, e.g. Freund, 2003, De  
14 Santis et al., 2019a, among others) does not explain any change on the parameters that control the  
15 generation of seismic ruptures using magnetic measurements. This lack of knowledge makes the complete  
16 link between sesimo-electromagnetism and classical seismology impossible. In this work, we approach  
17 this link using one of the key points that control seismic rupture and slip on the fault: friction force and  
18 stress drop. During this work we use the tectonic geometry and stress drop of Maule 2010 Mw8.8  
19 earthquake in order to base, develop and compare our analysis. Using this, in section 2 we develop the  
20 topic of friction coefficient adding the brittle-plastic stress changes contribution to the usual elastic stress.  
21 In section 3 we discuss the temporal changes of the brittle-plastic friction and the first implications of its  
22 spatial distribution on the fault and lithosphere. In section 4 is shown the stress drop in terms of the co-  
23 seismic magnetic field. The spatial-temporal friction coefficient along the fault is studied by adding the  
24 elastic stress drop. The Gutenberg-Richter's law is also written in terms of the semi brittle-plastic shear  
25 stress in section 5. The rupture time is discussed in section 6. Finally, the discussion and conclusion are  
26 shown in section 7.

27

## 28 **2.- Friction coefficient in the brittle-plastic regimen**

29

30 The standard friction force can be understood as the complex dissipation of mechanical energy in the form  
31 of plastic or elastic deformation of asperities (mechanical interaction), thermal dissipation (heat) and the  
32 adhesion (interatomic interaction) of two sliding surfaces (e.g. Sun and Mosleh, 1994). When we consider  
33 a particular contact area between two dry surfaces, the static friction coefficient  $\mu$  that describes this  
34 interaction can be written approximately as the ratio of shear  $\tau$  and normal  $N$  stress (load) as show  
35 Equation (1) (e.g. Byerlee, 1978, Chen, 2014, and references therein).

36

$$\mu = \frac{\tau}{N}. \quad (1)$$

37

38 The static friction coefficient  $\mu$  can give some information about the contact behavior. For instance,  $\mu$  tend  
39 to be high when the contact area is increased due to the surface's plastic deformation (e.g. Chen, 2014). If  
40 we also consider the pure plastic regimen, we can add a small plastic shear stress ( $\delta\tau_{plastic}$ ) and a small  
plastic normal stress ( $\delta N_{plastic}$ ) contribution in Equation (1) leading to the following expressions:

41

$$\tau = \tau_{elastic} + \delta\tau_{plastic}. \quad (2)$$

42

$$N = N_{elastic} + \delta N_{plastic}. \quad (3)$$

1 If we do not consider the pure plastic effects, the plastic contribution is vanished and the ratio of  
 2  $\tau_{elastic}$  and  $N_{elastic}$  describe the usual (non-linear) friction behaviors that occur during the complete  
 3 frictional cycle: Pre-Sliding (increase of friction coefficient when there is no-apparent or residual  
 4 displacement), Gross-Sliding (observable displacement and decrease of friction coefficient) and Healing  
 5 (friction coefficient recovery) (e.g., Parlitz et al., 2004, Marone and Saffer, 2015, Papangelo et al., 2015,  
 6 and references therein).

7 On the other hand, Venegas-Aravena et al. (2019) state that the electrification within rocks is mainly due  
 8 to a non-constant stress change during the semi brittle-plastic transition. This means that the temporal  
 9 changes of the semi brittle-plastic stress ( $\delta\sigma_{sbp}$ ) rules the total plastic stress ( $\delta\sigma_{plastic}$ ). Thus, it implies  
 10 that the plastic shear and normal stress can be written in terms of a linear combination of the temporal  
 11 changes of  $\delta\sigma_{sbp}$  as show Equation (4) and (5).

$$12 \quad \delta\tau_{plastic} = k_1\delta\tau_{sbp} + k_2\delta^2\tau_{sbp} + o(\delta^2\tau) = k_1 \dot{\tau}_{sbp}\delta t + k_2 \ddot{\tau}_{sbp}(\delta t)^2 + o((\delta t)^2), \quad (4)$$

$$14 \quad \delta N_{plastic} = k_3\delta N_{sbp} + k_4\delta^2 N_{sbp} + o(\delta^2 N) = k_3 \dot{N}_{sbp} \delta t + k_4 \ddot{N}_{sbp}(\delta t)^2 + o((\delta t)^2), \quad (5)$$

13

15 where  $k_1$ ,  $k_2$ ,  $k_3$  and  $k_4$  are dimensionless constants to determine,  $\delta t$  and  $(\delta t)^2$  are the temporal delta  
 16 from the first and second order time contribution. The temporal variations of the shear and normal semi  
 17 brittle-plastic stress contributions are  $\dot{\tau}_{sbp}$ ,  $\ddot{\tau}_{sbp}$ ,  $\dot{N}_{sbp}$  and  $\ddot{N}_{sbp}$  respectively. The expansion in Equations  
 18 (4) and (5) are convenient because they allow studying the plastic contribution as a sum of stresses that  
 19 depend on time. This is relevant because the seismic-electromagnetic theory seeks to relate the temporal  
 20 variable of earthquake prediction and stress within the lithosphere. Here and after we refer to the semi  
 21 brittle-plastic stress just as the uniaxial stress  $\sigma$ .

22 It is possible to relate this shear, and the normal stresses from Equations (4) – (5) with the uniaxial stress  
 23 using the geometry shown in Figure 1. In this Figure, it is possible to observe a simple schematic  
 24 representation of the lithosphere under uniaxial stress change  $d\sigma/dt$  in the presence of a fault with static  
 25 friction coefficient  $\mu$  and a dip angle of 30 degrees. We can write this uniaxial stress change in terms of  
 26 the dip angle  $\theta$ , normal and tangential direction (in red on Figure 1) of the fault, as shown in the following  
 27 expression

$$28 \quad \frac{d\sigma}{dt} = \frac{d\sigma}{dt} (-\sin \theta \hat{N} + \cos \theta \hat{\tau}), \quad (6)$$

29 where  $d\sigma/dt$  corresponds to the magnitude of uniaxial temporal stress change. Using this, we can write  
 30 the brittle-plastic stress contributions in term of uniaxial stress change as:

$$31 \quad \dot{N} = -\frac{d\sigma}{dt} \sin \theta. \quad (7)$$

$$32 \quad \dot{\tau} = \frac{d\sigma}{dt} \cos \theta. \quad (8)$$

33 Replacing the Equations (2) – (8) in Equation (1), and considering a second-order linear combination, we  
 34 can obtain the static friction coefficient as a function of time, the fault angle and the semi brittle-plastics  
 35 changes within lithosphere given by:

$$36 \quad \mu(t) \approx \frac{\tau_0 + (k_1 \dot{\sigma} + k_2 \ddot{\sigma} \delta t) \cos \theta \delta t}{N_0 - (k_3 \dot{\sigma} + k_4 \ddot{\sigma} \delta t) \sin \theta \delta t}, \quad (9)$$

37 where the dots above  $\sigma$  mean first and second temporal derivative of uniaxial stress. According to  
 38 Venegas-Aravena et al. (2019), the temporal stress change  $\dot{\sigma}$  has sigmoidal shape, which can be defined

1 as  $\dot{\sigma}(t) = a/(b + e^{(t_0-t)*w})$ , where  $a, b, w$  and  $t_0$  are constants. In Figure 2 we can see a dimensionless  
2 shape of  $\dot{\sigma}$  and  $\ddot{\sigma}$  as a function of time when we use  $a = b = w = 1$  and  $t_0 = 10$ . According to De Santis  
3 et al. (2019b), most of the earthquakes recorded occurred close to the center of the Figure 2, which is  
4 when  $t_{EQ} = t_0$ . For instance, Marchetti and Akhoondzadeh (2018) shown that the Mexico earthquake  
5 Mw8.2 occurred after this time ( $t_{EQ} > t_0$ ). They also use daily values of magnetic anomalies ( $B \propto \frac{d\sigma}{dt}$ ,  
6 which comes directly from the experimental equation:  $I = \alpha_0 \frac{d\sigma}{dt}$ , where  $I$  is the electric current and  $\alpha_0$  is a  
7 constant of proportionality ( e.g., Vallianatos, F. and Triantis and references therein )), thus  $\delta t = 1 \text{ day} =$   
8  $86400 \text{ s}$ .

9 Let us now, to figure out the values of constants of Equation (9). First, the dip or subduction angle  $\theta$  is  
10 needed. According to Maksymowicz (2015), this angle is close to 20 degrees at the depth ( $\sim 30 \text{ km}$ ) and  
11 location ( $35^\circ 54' 32''\text{S}$ ,  $72^\circ 43' 59''\text{W}$ ) of Maule 2010 earthquake. Maksymowicz (2015) claim that the static  
12 friction coefficient in the Chilean convergent margin is close  $\mu_{ch} \approx 0.5$ . Lamb (2006) calculate that the  
13 initial value of  $\tau_0$  is 15.4 MPa (constant) in southern Chile. Using  $\mu_{ch}$ , it is expected that  $N_0$  should be  
14 close to 30.8 MPa (constant).

15 On the other hand, rock experiments show that the values of  $\dot{\sigma}$  are close to 1 MP/s (e. g. Saltas et al.,  
16 (2018)). This implies that  $|k_1|$  and  $|k_3|$  must be close to  $\sim 10^{-4}$ , in order to balance the  $\delta t$  factor. The  
17 values of  $k_2$  and  $k_4$  must be equal or lesser than  $\sim 10^{-9}$ . Otherwise, the values of friction coefficient  
18 would be greater than 1. If we consider an initial increase of the normal stress, the sign of the constants  
19 should be negative for  $k_3, k_4$  and positive for  $k_1, k_2$ . In Figure 3 we can see how the friction coefficient  
20 changes in time, when using values of  $k_1$  and  $k_3$  described above, and different values of  $k_2$  and  $k_4$   
21 (second order contribution). When we use values of  $k_2$  and  $k_4$  similar to  $\sim 10^{-9}$ , it's possible to observe  
22 how the friction decreases after the earthquake. Furthermore, it's important to note that the earthquake  
23 does not occur when the friction has its maximum value, but occurs close to it. When we use values of  
24  $k_2$  and  $k_4$  similar or lesser than  $\sim 10^{-10}$  the contribution of  $\dot{\sigma}$  in Equation (9) is vanished.

25 Another critical point is related to the differential time. For instance, when we consider  $\delta t \leq 1 \text{ s}$ , implies  
26 that the semi brittle-plastic stress term vanishes due to the values of the parameters and the usual friction  
27 are recovered. This fact is especially notable because the semi brittle-plastic contribution to the friction  
28 coefficient seems to be relevant only during long periods. In other words, the friction coefficient of  
29 Equation (9) could be view as a generalization of the standard friction when long periods are considered.

### 30 31 32 **3.- Spatial distribution of stress changes and friction** 33

34 In the previous section it was possible to link the friction coefficient to the semi brittle-plastic regimen that  
35 generates microcracks and electrification within the rocks. However, ~~this phenomena seems not to~~ occur  
36 everywhere. For instance, Dobrovolsky et al. (1979) described a specific "preparation zone" required close  
37 to the future hypocenter in order to accumulate sufficient stress to triggers the earthquake. This criterion  
38 has been widely used by modern researchers to establish a limit where the magnetic measurements can be  
39 associated to earthquakes (e.g. De Santis et al., 2019a, De Santis et al., 2019b). In other words, this  
40 phenomena is local. However, if this is applied, a variation of the friction coefficient related to the rock  
41 electrification phenomena close to the fault would be expected, while a friction variation outside zones of  
42 semi brittle-plastic influence ~~would not be~~.

43 In order to consider this feature, we can add a spatial function to the uniaxial stress as  $\bar{\sigma}(x, t) = \gamma(x)\sigma(t)$   
44 (for simplicity we choose only the x direction). Where  $\sigma(t)$  correspond to the same uniaxial stress  
45 considered before and  $\gamma(x)$  is the dimensionless spatial distribution parallel to the fault (see the coordinate

1 system in Figure 4). Furthermore, the values of  $\gamma(x)$  must be different when constant and non-constant  
 2 stress changes are considered. With this, we can re-write Equation (9) as:

$$3 \quad \bar{\mu}(x, t) \approx \frac{\tau_0 + \gamma(k_1 \dot{\sigma} + k_2 \ddot{\sigma} \delta t) \cos \theta \delta t}{N_0 - \gamma(k_3 \dot{\sigma} + k_4 \ddot{\sigma} \delta t) \sin \theta \delta t}. \quad (10)$$

4 Furthermore, after straightforward calculations, we can calculate the gradient of the friction coefficient  
 5 along the fault using Equation (10) as:

$$6 \quad \nabla \bar{\mu}(x, t) = \gamma' \frac{AN_0 + B\tau_0}{(N_0 - \gamma B)^2} = \gamma' \frac{\alpha \dot{\sigma} \delta t + \beta \ddot{\sigma} \delta t^2}{(N_0 - \gamma B)^2}, \quad (11)$$

7 where  $A = (k_1 \dot{\sigma} + k_2 \ddot{\sigma} \delta t) \cos \theta \delta t$ ,  $B = (k_3 \dot{\sigma} + k_4 \ddot{\sigma} \delta t) \sin \theta \delta t$ ,  $\alpha = N_0 k_1 \cos \theta + \tau_0 k_3 \sin \theta$  and  
 8  $\beta = N_0 k_2 \cos \theta + \tau_0 k_4 \sin \theta$ . Equation (10) and (11) imply that if we distribute the constant and non-  
 9 constant temporal stress change in a non-uniform manner along the fault, then, it could be said that this  
 10 phenomenon is local. This can be understood using the example of Figure 4: The Figure 4a shows a blue  
 11 area of length L where it is applied a non-constant temporal stress change. Then, it is expected that the  
 12 fault suffers a change in the friction coefficient inside the projected gray area (Figure 4b). On the other  
 13 hand, if we consider that there is a constant stress change outside the area of length L, (Figure 4c), then we  
 14 would not expect any change in the friction coefficient (Figure 4d). It's important to keep in mind that the  
 15 entire fault suffered from stress accumulation during the entire example. However, only the grey area  
 16 could be affected by the friction change. This example also shows that the temporal friction changes are  
 17 restricted only to a specific area (grey area) on the fault. Hence, must exist a non-zero friction coefficient  
 18 gradient on the fault to have a local phenomenon ( $\nabla \bar{\mu} \neq 0 \Leftrightarrow Local$ ).

19

20 The example of Figure 4 reveals why it is expected that magnetic measurements are not a global  
 21 phenomenon and also validate the locality criteria in terms of fault properties. Furthermore, the spatial  
 22 distribution of magnetic ~~measurements~~ is expected to be comparable to the spatial length of change in the  
 23 friction coefficient due to the dependency of  $\gamma(x)$  in Equation (10). That is the larger detection area of  
 24 magnetic anomalies, the higher the area where fault friction is changing. In addition, Venegas-Aravena et  
 25 al. (2019) describe how the uniaxial stress change implies a change in the b-value of the Gutenberg-  
 26 Richter Law. It also implies that a significant earthquake is needed in order to satisfy this change in the  
 27 Gutenberg-Richter Law. ~~Hence, the greater magnitude (and amount of earthquakes) expected could be~~  
 28 ~~related to the changes in the frictional coefficient within localized areas on the fault.~~ However, changes in  
 29 the friction coefficient do not directly implies the earthquakes generation itself.

30

#### 31 **4.- Stress drop and Total friction coefficient: Spatial-temporal behavior**

32

33 Up to this moment, no changes in the elastic stresses have been considered in Equation (10). ~~Because of~~  
 34 ~~that, this section is~~ studies one of the elastic parameters that are involved in the seismic rupture process:  
 35 the stress drop  $\Delta\tau$ . This parameter is one of the most relevant because it show the shear stress differences  
 36 prior to and after the earthquake event within the fault rupture area (e.g. Aki, 1966). Furthermore, it can be  
 37 also linked with the seismic waves radiated (through the corner frequency of waves) and the seismic  
 38 moment  $M_0$  (e.g. Eshelby, 1957, Brune, 1970, Baltay et al., 2011, and references therein). If we consider  
 39 a circular rupture area with radius  $d_{crack}$ , the stress drop  $\Delta\tau$  is linked with the seismic moment  $M_0$  through  
 40 the following equation (Eshelby, 1957).

$$\Delta\tau = \frac{7}{16} \frac{M_0}{d_{crack}^3}. \quad (12)$$

On the other hand, the seismic moment  $M_0$  and moment magnitude  $Mw$  in terms of the co-seismic magnetic field can be related. Hence, the seismic moment is given by:

$$M_0 \approx \mu_{sm} \frac{B_{cs} r^2 (3-D)}{\mu_m J D(D-2)} (l_{min}^{2-D})(l_{max}^{D-3})d, \quad (13)$$

where  $\mu_{sm}$  is the shear modulus,  $d$  the average slip,  $D$  fractal dimension of rock,  $B_{cs}$  the co-seismic magnetic field,  $J$  corresponds to the total electric current density,  $\mu_m$  is the magnetic permeability of the medium,  $r$  the distance to the fault,  $l_{max}$  and  $l_{min}$  are the radius of the circular rupture area and the smallest microcrack length, respectively. The circular rupture is calculated using  $l_{max} = \sqrt{S/\pi}$ , where  $S$  corresponds to the total rupture area.

In this case, the rupture geometry is circular in both formulations, thus,  $d_{crack} = l_{max}$ . Replacing this into Equation (13) and Equation (12):

$$\Delta\tau \approx \frac{7}{16} \mu_{sm} \frac{B_{cs} r^2 (3-D)}{\mu_m J D(D-2)} (l_{min}^{2-D})(l_{max}^{D-6})d. \quad (14)$$

Equation (14) relates the stress drop with the co-seismic magnetic measurements, seismic rupture, and the electrical and mechanical properties of rocks (lithosphere). We can use the data from the Maule earthquake in order to contrast the result of Equation (14) with those found by other researchers. If we use the fault values:  $\mu_{sm} = 3.3 \times 10^{10} Pa$ ,  $d = 4 m$  and  $S = 450 \times 120 km^2$  (Vigny et al., 2011; Yue et al., 2014), the granite rock and brittle properties:  $\mu_m = 13.5 \times 10^{-7} NA^{-2}$  (Scott, 1983),  $J = 5 \times 10^{-6} Am^{-2}$  (Tzanis and Vallianatos, 2002),  $l_{min} = 10^{-3} m$  (Shah, 2011) and  $D = 2.6$  (Turcotte, 1997). The magnetic data  $B_{cs} \approx 0.1 nT$  at  $r \approx 250 km$  (Figure 5 in Venegas-Aravena et al. (2019)), we obtain a stress drop  $\Delta\tau \approx 3.4 MPa$ . This result is close similar to the result of Luttrell et al. (2011) (4 MPa). Using this, we can calculate the elastic shear stress as:

$$\tau_{elastic} = \tau_0 - \gamma_2 \Delta\tau H(t - t_0), \quad (15)$$

where  $H(t - t_0)$  correspond to the step function centered at  $t_0$  (the time when the earthquake occurs) and  $\gamma_2$  is a second step function that represents the fault area where exist the stress drop. This means that if  $\gamma_2 = 0$  if is considered a point outside the rupture area, and  $\gamma_2 = 1$  if the point is within the rupture area. Adding this result to Equation (10), we are able to calculate the total friction coefficient  $\bar{\mu}_T$  of fault as:

$$\bar{\mu}_T(x, t) \approx \frac{\tau_0 - \gamma_2 \Delta\tau H(t - t_0) + \gamma(k_1 \dot{\sigma} + k_2 \ddot{\sigma} \delta t) \cos \theta \delta t}{N_0 - \gamma(k_3 \dot{\sigma} + k_4 \ddot{\sigma} \delta t) \sin \theta \delta t}. \quad (16)$$

This total friction coefficient  $\bar{\mu}_T$  is especially relevant because of the dependence of the co-seismic magnetic measurements  $B_{cs}$  (through the stress drop  $\Delta\tau$ ) and the magnetic anomalies (through the relation  $B \propto \dot{\sigma}$ ). Furthermore, Equation (16) explains the spatial distribution of friction along the fault in addition to the time variations. In this Equation, it is also clear that the spatial changes of friction (represented by  $\gamma$ ) are not necessarily related to the seismic rupture area (represented by  $\gamma_2$ ). However, in the case that if they are really related, it is expected that  $\gamma_2$  would be a function of  $\gamma$  (or vice versa). That is  $\gamma_2 = \gamma_2(\gamma(x))$ . The general case of total friction coefficient gradient can be written as:

$$\nabla \bar{\mu}_T = \nabla \bar{\mu} + \Delta\tau H(t - t_0) \Gamma(\gamma, \gamma_2), \quad (17)$$

where  $\Gamma(\gamma, \gamma_2) = \frac{1}{(N_0 - \gamma B)^2} [\gamma_2'(\gamma B - N_0) - \gamma' \gamma_2 B]$ ,  $\nabla \bar{\mu}$  is the friction gradient defined in Equation (11), and the same definition of  $A$  and  $B$  are used. The second term of Equation (17) implies that more complex

1 spatial friction distribution on the fault is expected after the earthquake. When no brittle-plastic  
 2 contribution is considered ( $\gamma = 0$ ), the friction is only proportional to the gradient of fault rupture  
 3 distribution ( $\nabla\bar{\mu}_T = -\Delta\tau H(t - t_0)\gamma'_2/N_0$ ). When  $\gamma_2 \approx \gamma$ , the two terms of the Total Friction Coefficient  
 4 will be proportional to the spatial distribution gradient ( $\nabla\bar{\mu}_T \propto \gamma'$ ). If the earthquake does not occur, the  
 5 second term vanishes and the Equation (11) is recovered.

6 On the other hand, if we consider one point affected by the rupture area, and the same values needed to  
 7 create the Figure 3, we can calculate the shape of the total friction coefficient as is shown in Figure 5. The  
 8 three cases show the increase of friction coefficient prior the earthquake, and in the three cases the friction  
 9 reach it maximum values before the earthquake ( $t=10$ ). The decrease is due the stress drop influence  
 10 calculated using the co-seismic magnetic field  $B_{CS}$ . After the earthquake, in none of the cases, the friction  
 11 is completely recovered to values instantly before the earthquake.

12 Furthermore, it is also possible to compare the temporal behavior of the friction coefficient in terms of the  
 13 fault point choose. For instance, in Figure 6 (above) is shown the different friction behavior expected if we  
 14 consider the Total friction coefficient. There it is also pointed out the seismic rupture (blue area) influence  
 15 in terms of the stress drop. This stress drop is not expected out the seismic rupture, however, still is  
 16 possible to observe differences in the friction behavior at the point close to the rupture (yellow area) in the  
 17 case  $\gamma_2 \neq \gamma$ . In Figure 6 (bottom), the standard friction drop is expected at the rupture area. However, a  
 18 non-measurable change in friction is observed prior to the earthquake.

19 We can quantify this analysis using two different distribution of  $\gamma$  and  $\gamma_2$ . For instance, in Figure 7 is  
 20 shown the double-sigmoidal distribution for  $\gamma$  and  $\gamma_2$  (black and red curves respectively) along the fault x-  
 21 direction (of total length  $2x_{half}$ ). The dimensionless distribution is defined as a combination of sigmoidal  
 22 function used in the section 2 as:

$$23 \quad \gamma(x), \gamma_2(x) = \begin{cases} \frac{a}{b - e^{(x_0-x)*w}}, & x < x_{half} \\ 1 - \frac{a}{b - e^{(x_0+L-x)*w}}, & x \geq x_{half} \end{cases} \quad (18)$$

24 If we consider  $a = b = 1$  and  $x_{half} = 10$  in both distributions, and  $x_0 = 5, L = 10$  and  $w = 1$  for  $\gamma$  and  
 25  $x_0 = 8, L = 4$  and  $w = 10$  for  $\gamma_2$ , we can create the two distributions of Figure 7. These values show the  
 26 same scenario discuss in Figure 6. That is a rupture length ( $L = 4$  in  $\gamma_2$  represent the x-direction of the red  
 27 area in Figure 6) lesser than the friction coefficient influenced by semi brittle-plastic stress (here  $L =$   
 28  $10$  in  $\gamma$  represent the x-direction of the yellow area in Figure 6). Using both sets of values, those used in  
 29 the stress drop (Equation (14)) and also the same  $k$ -parameters used in Equation (9), it is possible to  
 30 calculate the total friction coefficient (Equation (16)) as shown the Figure 8 (case  $k_2 = k_4 = 10^{-9}$ ). At  
 31 time  $t = 0$ , no friction changes occur ( $\bar{\mu}_T = 0.5$ ). However, the friction increase begins close to  $t=5$ , where  
 32 the spatial distribution  $\gamma$  is initially defined as non-zero ( $x \in [5, 15]$ ). The friction increases up to  $t=10$ , the  
 33 time where the earthquake occurs. The earthquake rupture length is shown as a sudden friction decrease  
 34 ( $x \in [8, 12]$ ) from 0.76 to 0.67. In the zone immediately close to the rupture, the friction increases even  
 35 more up to the maximum values (0.77), while the rupture section decreases the friction. After this time  
 36 ( $t \sim 12$ ), the rupture and surrounding section have a friction decrease.

37 The case of  $k_2 = k_4 = 10^{-10}$  is shown in Figure 9. The rupture is shown as a blue area at  $t=10$  in  
 38 section  $x \in [8, 12]$ . At this time and location it is possible to observe that friction decreases to similar  
 39 initial values ( $\sim 0.5$ ). The friction of this rupture section increase after the earthquake up to  $\sim 0.6$ . On the  
 40 other hand, the rupture's surrounding section increases up to the maximum values ( $\sim 0.7$ ). Despite of this,  
 41 the initial ( $t=0$ ) and final ( $t=20$ ) friction values are almost similar for both cases. For instance, the rupture  
 42 area has values close to 0.6 in Figures 8 and 9. The surrounding rupture section has values close to 0.69 in

1 both cases and the section away from the rupture (close to  $x=0$  and  $x=20$ ) always has the same initial  
 2 value (0.5) in both cases. Besides, both cases exhibit a complex behavior after de earthquake occurs, as  
 3 Equation (17) reveals.

4 On the other hand, when the semi brittle-plastic contribution is not considered, it implies that  $\gamma = 0$ . The  
 5 result is shown in Figure 10 and is only observed the sudden friction decrease at  $t=10$  (and  $x \in [8, 12]$ ).  
 6 Furthermore, not any other complex friction behavior is observed.

## 8 5.- The semi brittle-plastic Gutenberg-Richter law

10 A general expression for friction has been obtained in Equation (16). Moreover, it is possible to study the  
 11 Gutenberg-Richter's law in this semi brittle-plastic context. This law establishes a relation between the  
 12 number of earthquakes that exist in a region and the magnitude of them (Gutenberg and Richter, 1944).  
 13 Mathematically, this link is written as:  $\log N = a - b \times m$ . Where  $N$  is the number of earthquakes with  
 14 magnitude equal to or greater than  $m$ , and  $a$  and  $b$  are constants. However, the b-value of this law might  
 15 evolve and not be constant on time. On the other hand, De Santis et al. (2011) determined an equation that  
 16 relate the temporal evolution of b-value ( $b = b(t)$ ) and the measure of the stress  $H(t)$  of that region  
 17 as  $b(t) = b_{max} 10^{-H(t)}$ , where  $b_{max} = e \log_{10} e$ . This stress measurement  $H(t)$  can be proportional to the  
 18 real stress in the lithosphere (Venegas-Aravena et al., 2019). If we consider the total shear stress  $\tau_T$  in the  
 19 fault described by Equation (16), we can write:

$$20 \quad b(t) = b_{max} 10^{-k_0 \tau_T}, \quad (19)$$

21 where  $\tau_T = \tau_0 - \gamma_2 \Delta \tau H(t - t_0) + \gamma(k_1 \dot{\sigma} + k_2 \ddot{\sigma} \delta t) \cos \theta \delta t$  and  $k_0$  is a constant in units of inverse  
 22 stress. If we use the same values that were used to create Figure 5 ( $k_2 = k_4 = 10^{-9}$ ), we can find the  
 23 temporal evolution of the b-value (Figure 11a). Figure 11a shows a decrease in b-value until the  
 24 earthquake occurs ( $t=10$ ). Figure 11b shows the Gutenberg-Richter's law for three instants of time  
 25 (and  $k_0 = 0.01$ ,  $a=1$ ): initial ( $t=0$ ), prior to the earthquake ( $t=9$ ) and final ( $t=20$ ). This Figure shows how  
 26 large earthquakes ( $M_w \sim 6$ ) are not expected at the initial moment (blue line). However, just before the  
 27 earthquake, an M8-class earthquake should be expected (green line). After the earthquake one would only  
 28 expect earthquakes no greater than  $M_w \sim 7$  to exist (red line). Figure 12a and 12b show the same previous  
 29 case but considering  $k_2 = k_4 = 10^{-10}$ . In this case there are no differences between time, immediately  
 30 before the earthquake ( $t=9$ ) and at the end time ( $t=20$ ). In addition, using these parameters ( $k_2 = k_4 =$   
 31  $10^{-10}$ ), smaller magnitudes are reached than using  $k_2 = k_4 = 10^{-9}$  ( $M_w \sim 7$  and  $M_w \sim 8$  respectively).  
 32 This is why it is more likely to find earthquakes of greater magnitude when considering the contribution  
 33 of  $\ddot{\sigma}$  within analyzes.

## 35 6.- Rupture time $t_0$

36 In section 5 it was found that  $k_2 = k_4 = 10^{-9}$  values were more adequate. Despite this, the Gutenberg-  
 37 Richter law does not give us an approximate time  $t_0$  for the earthquake occurrences. If we look at  
 38 Equation (16), the term  $t_0$  appears explicitly (step function). However,  $t_0$  appears only after the  
 39 earthquake, so it is not possible to find  $t_0$  analytically before the rupture (using the rupture itself). This  
 40 means that we must find an approximate expression from other parameters. For example, if we consider  
 41 the differential total friction coefficient  $d\bar{\mu}_T$  it is possible to find approximate rupture time  $t_0$ . Figure 13  
 42 shows  $d\bar{\mu}_T$  considering  $\gamma_2 = \gamma = 1$ ,  $k_2 = k_4 = 10^{-9}$  and  $k_2 = k_4 = 10^{-10}$ . When major earthquakes  
 43 expected ( $k_2 = k_4 = 10^{-9}$ ) are considered, the rupture occurs after the maximum value ( $(d\bar{\mu}_T)_{MAX}$ ),

1 when  $d\bar{\mu}_T \approx \frac{1}{2} (d\bar{\mu}_T)_{MAX}$  (Figure 13 up). When  $k_2, k_4 = 10^{-10}$ , the rupture also occurs after the  
 2 maximum value, different to the case in which  $d\bar{\mu}_T \approx 0.9 (d\bar{\mu}_T)_{MAX}$  (Figure 13 down). Considering  
 3 these two cases within this theory, we can write that earthquakes occur after  $(d\bar{\mu}_T)_{MAX}$  when the  
 4 differential total friction coefficient decrease to  $d\bar{\mu}_T \approx C (d\bar{\mu}_T)_{MAX}$ , where  $C \in [0.5, 0.9]$ .

5 On the other hand, the time between  $d\bar{\mu}_T \approx (d\bar{\mu}_T)_{MAX}$  and  $d\bar{\mu}_T \approx C (d\bar{\mu}_T)_{MAX}$  can be represented as  $\delta$ .  
 6 This  $\delta$  parameter increases when C decreases and viceversa, so  $\delta$  is inversely proportional to C ( $\delta \propto C^{-1}$ ).  
 7 Then, we can write the general rupture time  $t_0$  as:

$$8 \quad t_0 \approx t_{C (d\bar{\mu}_T)_{MAX}} = t_{(d\bar{\mu}_T)_{MAX}} + \delta, \quad t > t_{(d\bar{\mu}_T)_{MAX}}, \quad (20)$$

9 where  $t_{(d\bar{\mu}_T)_{MAX}}$  is the time when  $d\bar{\mu}_T \approx (d\bar{\mu}_T)_{MAX}$ . Note that the Equation (20) is only valid after the  
 10 maximum value  $(d\bar{\mu}_T)_{MAX}$  is reached. Equation (20) is general, however, considering the Gutenberg-  
 11 Richter law, it would be expected that C values close to 0.5 are necessary to represent earthquakes of  
 12 greater magnitude in this theory.

13

## 14 7.- Discussion and conclusions

15

16 ~~In this work it was possible to relate one of the properties of the key faults to the magnetic measurements.~~  
 17 Both stress drops and the semi brittle-plastic stress were linked to friction coefficient (on the fault)  
 18 equation in terms of magnetic measurements (Equation (16)). One of the critical points of Equation (16)  
 19 corresponds to the fact that the Total Friction Coefficient  $\bar{\mu}_T(x, t)$  is entirely determined by the spatial  
 20 distribution of the non-constant stress changes within the lithosphere. If the Seismo-electromagnetic  
 21 theory is applied, it implies that the rupture process might be controlled by the non-constant stress changes  
 22 that surround the fault and not entirely by the fault itself. In this scenario, the earthquakes might occur at  
 23 places on the fault that are being affected by a continuous friction increase prior to rupture (this friction  
 24 increase occur regardless of the values of  $k_2$  and  $k_4$  used). However, the Total Friction Coefficient  
 25 depends on two different spatial distribution. The first one is associated with the uniaxial stress  
 26 changes  $\gamma(x)$  and the second one to the rupture area  $\gamma_2(x)$ . This two distribution are not necessarily  
 27 correlated. In the case that both are comparable (that is:  $|\gamma(x) - \gamma_2(x)| \approx 0$ ), it could mean that the  
 28 lithosphere area affected by non-constant uniaxial stress changes could determine the earthquake  
 29 magnitude and location before it occurs. This is  $\gamma(x) \approx \gamma_2(x) \approx 0$  if  $x$  belong to sections where  $\dot{\sigma} = cte$   
 30 and  $\gamma(x), \gamma_2(x) \neq 0$  if  $x \in L$ , where  $L$  is the rupture length (places where  $\dot{\sigma} \neq cte$ ). The seismic moment  
 31  $M_0$  is proportional to this length  $L$  (Aki, 1966), and the seismic moment magnitude  $M_w$  depend on the  
 32 seismic moment (Hanks and Kanamori, 1979), implying that the seismic moment magnitude could depend  
 33 on the spatial distribution of the total friction coefficient increases. As the non-constant uniaxial stress  
 34 changes also could create magnetic signals due the microcracks of rocks (Venegas-Aravena et al., 2019,  
 35 and references therein), it is valid to say that a larger area of magnetic anomaly ~~measurements~~  
 36 a larger earthquake. This is the locality (Dobrovolsky) criteria used by some researchers when they try to  
 37 relate some electromagnetic measurements to earthquakes (e.g., De Santis et al., 2019a, and references  
 38 therein). If in this case we also consider the initial time of friction increase (impending rupture time), the  
 39 approximate magnitude, the approximate location and the approximate imminent time could be  
 40 theoretically determined.

41 On the other hand, if  $|\gamma(x) - \gamma_2(x)| \gg 0$  implies that the locality criteria does not hold anymore. Hence,  
 42 the earthquakes occurrences should not be related to the non-constant stress changes and the magnetic  
 43 measurements. Furthermore, this case also closes the possibility of a real earthquake prediction using this  
 44 theoretical base. This case may also imply that the cumulative stress on the fault is not enough to generate  
 45 a seismic rupture at any point on the fault (this is  $\gamma_2(x) = 0$ ). This means that the semi brittle-plastic

1 energy injected to the fault is lesser than the Fracture Energy  $G$  (The energy required to spread a rupture,  
2 e.g., Nielsen et al., 2016, and references therein). The last scenario could indicate that the stress changes  
3 are not a sufficient condition to the earthquake generation, however, it could be a necessary condition.

4 With respect to the size of earthquakes in this model, the section 5 revealed that earthquakes may have  
5 greater magnitudes when  $k_2 = k_4 \approx 10^{-9}$ . If we consider those values in Figure 5, we can see that the  
6 total friction coefficient is also higher. This is  $\sim 0.75$  when  $k_2 = k_4 \approx 10^{-9}$  and  $\sim 0.6$  when  $k_2 = k_4 \approx$   
7  $10^{-10}$ . This indicates that there could be also a correlation between the size of the earthquake and the total  
8 friction coefficient. Hence, the earthquake has a greater magnitude when there is a higher total friction  
9 coefficient (or shear stress  $\tau$ ). This means that  $\gamma_2 = \gamma_2(\bar{\mu}_T)$ , therefore, the rupture length  $L$  of Equation  
10 (18) is proportional to  $\bar{\mu}_T$  (that is:  $L = \alpha \bar{\mu}_T(t_0)$ ). Note that this is independent of the value of  $|\gamma(x) -$   
11  $\gamma_2(x)|$ , since it comes directly from the Gutenberg-Richter's law. However, in this case  $\bar{\mu}_T$  is  
12 homogeneous, so more studies will be needed when it is not to calculate  $L$ .

13 Finally, this theoretical work has shown a possible mechanism that explains several magnetic  
14 measurements performed during the last years. Furthermore, it has also been possible to perform some  
15 studies that reveal the possible necessary conditions of the fault to trigger earthquakes in terms of the  
16 magnetic properties. Hence, future investigations of the LAIC effect community should also be focused on  
17 the lithospheric-fault dynamics as one of the main topics. When the lithosphere part of this effect would  
18 be understood, the others effects will have a strong theoretical base in order to perform measurements  
19 and/or any predictions.

## 21 **Acknowledgments**

22  
23 In memory of Marcela Larenas Clerc (1960-2019). P.V.-A. acknowledges Patricia Aravena, Alejandro  
24 Venegas, Patricia Venegas and Richard Sandoval for outstanding support to carry out this work, and  
25 Valeria Becerra-Carreño for her scientific support. D. L. acknowledges partial financial support from  
26 Centers of excellence with BASAL/CONICYT financing, grant FB0807, CEDENNA.  
27  
28

1 **References**

2  
3  
4 Aki, K.: Generation and propagation of G waves from the Niigata earthquake of June 14, 1964. Part 2.  
5 Estimation of earthquake moment, released energy and stress-strain drop from G wave spectrum. Bulletin  
6 of the Earthquake Research Institute, 44: 73–88, 1966.

7  
8 Anastasiadis, C., Triantis, D., Stavrakas, I. and Vallianatos, F.: Pressure Stimulated Currents (PSC) in  
9 marble samples. *Ann. Geophys.*, 47, 1, pp. 21-28, 2004.

10  
11 Baltay, A., Ide, S., Prieto, G. and Beroza, G.: Variability in earthquake stress drop and apparent stress.  
12 *Geophysical Research Letters*. VOL. 38, L06303, doi:10.1029/2011GL046698, 2011.

13  
14 Brune, J. N.: Tectonic stress and the spectra of seismic shear waves from earthquakes, *J. Geophys. Res.*,  
15 75(26), 4997–5009, doi:10.1029/JB075i026p04997, 1970.

16  
17 Byerlee, J.D.: Friction of Rocks. *Pure and Applied Geophysics*. 116 (4–5): 615–626.  
18 doi:10.1007/BF00876528, 1978.

19  
20 Chen, G.S.: Fundamentals of contact mechanics and friction. *Handbook of Friction-Vibration Interactions*,  
21 71–152. doi:10.1533/9780857094599.71, 2014.

22  
23 Cordaro, E.G., Venegas, P. and Laroze, D.: Latitudinal variation rate of geomagnetic cutoff rigidity in the  
24 active Chilean convergent margin. *Ann. Geophys.*, 36, 275–285, [https://doi.org/10.5194/angeo-36-275-](https://doi.org/10.5194/angeo-36-275-2018)  
25 2018, 2018.

26  
27 De Santis, A., Cianchini, G., Favali, P., Beranzoli, L., and Boschi, E.: The Gutenberg–Richter Law and  
28 Entropy of Earthquakes: Two Case Studies in Central Italy, *B. Seismol. Soc. Am.*, 101, 1386–1395,  
29 <https://doi.org/10.1785/0120090390>, 2011.

30  
31 De Santis, A., Abbattista, C., Alfonsi, L., Amoroso, L., Campuzano, S.A., Carbone, M., Cesaroni, C.,  
32 Cianchini, G., De Franceschi, G., De Santis, A., Di Giovambattista, R., Marchetti, D., Martino, L.,  
33 Perrone, L., Piscini, A., Rainone, M.L., Soldani, M., Spogli, L. and Santoro, F.: Geosystemics View of  
34 Earthquakes, *Entropy*2019,21, 412; doi:10.3390/e21040412, 2019a.

35  
36 De Santis, A.; Marchetti, D.; Spogli, L.; Cianchini, G.; Pavón-Carrasco, F.J.; Franceschi, G.D.; Di  
37 Giovambattista, R.; Perrone, L.; Qamili, E.; Cesaroni, C.; De Santis, A.; Ippolito, A.; Piscini, A.;  
38 Campuzano, S.A.; Sabbagh, D.; Amoroso, L.; Carbone, M.; Santoro, F.; Abbattista, C.; Drimaco, D.:  
39 Magnetic Field and Electron Density Data Analysis from Swarm Satellites Searching for Ionospheric  
40 Effects by Great Earthquakes: 12 Case Studies from 2014 to 2016. *Atmosphere* 2019, 10, 371, 2019b.  
41

- 1 Dobrovolsky I.R., Zubkov S.I. and Myachkin V.I.: Estimation of the size of earthquake preparation  
2 zones. *Pure Appl. Geophys.* Volume 117, Issue 5, pp1025–1044. doi:10.1007/BF00876083, 1979.  
3
- 4 Eshelby, J. D.: The determination of the elastic field of an ellipsoidal inclusion, and related problems,  
5 *Proc. R. Soc. Lond. A. Math. Phys. Sci.*, 376–396, doi:10.1098/rspa.1983.0054, 1957.  
6
- 7 Freund, F.: Rocks That Crackle and Sparkle and Glow: Strange Pre-Earthquake Phenomena. *Journal of*  
8 *Scientific Exploration*, Vol. 17, No. 1, pp. 37–71, 2003.  
9
- 10 Gutenberg, B. and Richter, C. F.: Frequency of earthquakes in California, *B. Seismol. Soc. Am.*, 34, 185–  
11 188, 1944.  
12
- 13 Hanks, T. C. and Kanamori, H.: A moment magnitude scale, *J. Geophys. Res.*, 84, 2348–2350,  
14 <https://doi.org/10.1029/JB084iB05p02348>, 1979  
15
- 16 Luttrell, K. M., Tong, X., Sandwell, D.T., Brooks, B.A. and Bevis, M.G.: Estimates of stress drop and  
17 crustal tectonic stress from the 27 February 2010 Maule, Chile, earthquake: Implications for fault strength,  
18 *J. Geophys. Res.*, 116, B11401, doi:10.1029/2011JB008509, 2011.  
19
- 20 Maksymowicz, A.: The geometry of the Chilean continental wedge: Tectonic segmentation of subduction  
21 processes off Chile. *Tectonophysics* 659 (2015) 183–196, doi: 10.1016/j.tecto.2015.08.007, 2015.  
22
- 23 Marchetti, D. and Akhoondzadeh, M.: Analysis of Swarm satellites data showing seismo-ionospheric  
24 anomalies around the time of the strong Mexico (Mw = 8.2) earthquake of 08 September 2017. *Advances*  
25 *in Space Research* 62 (2018) 614–623, <https://doi.org/10.1016/j.asr.2018.04.043>, 2018.  
26
- 27 Marone, C. J. and Saffer, D.M.: The Mechanics of Frictional Healing and Slip Instability During the  
28 Seismic Cycle, *Treatise on Geophysics: Second Edition*, 4 , pp. 111-138. DOI: 10.1016/B978-0-444-  
29 53802-4.00092-0, 2015.  
30
- 31 Nielsen, S., Spagnuolo, E., Violay, M., Smith, S., Di Toro, G. and Bistacchi, A.: G: Fracture energy,  
32 friction and dissipation in earthquakes. *J. Seismol.* (2016) 20:1187–1205, DOI 10.1007/s10950-016-9560-  
33 1, 2016.  
34
- 35 Papangelo, A., Ciavarella, M. and Barber, J. R.: Fracture mechanics implications for apparent static  
36 friction coefficient in contact problems involving slip-weakening laws471*Proc. R. Soc. A*  
37 <http://doi.org/10.1098/rspa.2015.0271>, 2015.  
38
- 39 Parlitz, U., Hornstein, A., Engster, D., Al-Bender, F., Lampaert, V., Tjahjowidodo, T., Fassois, S.D.,  
40 Rizos, D., Wong, C.X., Worden, K. and Manson, G.: Identification of pre-sliding friction dynamics,  
41 *Chaos* 14, 420–430 (2004). <https://doi.org/10.1063/1.1737818>, 2004.

1  
2  
3  
4  
5  
6  
7  
8  
9  
10  
11  
12  
13  
14  
15  
16  
17  
18  
19  
20  
21  
22  
23  
24  
25  
26  
27  
28  
29  
30  
31  
32  
33  
34  
35  
36  
37  
38  
39

Potirakis, S.M., Contoyiannis, Y., Asano, T. and Hayakawa, M.: Intermittency-induced criticality in the lower ionosphere prior to the 2016 Kumamoto earthquakes as embedded in the VLF propagation data observed at multiple stations. *Tectonophysics*, 722, 422-431. 2018a.

Potirakis, S.M., Asano, T. and Hayakawa, M.: Criticality Analysis of the Lower Ionosphere Perturbations Prior to the 2016 Kumamoto (Japan) Earthquakes as Based on VLF Electromagnetic Wave Propagation Data Observed at Multiple Stations. *Entropy* 2018, 20, 199; doi: 10.3390/e20030199, 2018b.

Saltas V., Vallianatos F., Triantis D. and Stavrakas I.: Complexity in Laboratory Seismology. *Complexity of Seismic Time Series*, pages 239-273, 2018.

Scott, J.H.: Electrical and Magnetic properties of rock and soil. UNITED STATES DEPARTMENT OF THE INTERIOR GEOLOGICAL SURVEY. USGS Open-File Report 83-915, 1983.

Schekotov, A. and Hayakawa, M.: Seismo-meteo-electromagnetic phenomena observed during a 5-year interval around the 2011 Tohoku earthquake. *Physics and Chemistry of the Earth*, 85–86, 167-173, <http://dx.doi.org/10.1016/j.pce.2015.01.010>, 2015.

Shah, K. P.: The Hand Book on Mechanical Maintenance. Practical Maintenance. Compiled by: K P Shah. <http://practicalmaintenance.net/?p=1135>, 2011.

Sun, N. P., & Mosleh, M.: The Minimum Coefficient of Friction: What Is It? *CIRP Annals*, 43(1), 491–495. doi:10.1016/s0007-8506(07)62260-4, 1994.

Turcotte, D. L.: *Fractals and Chaos in Geology and Geophysics*, Cambridge University Press, Second edition, 397 p., 1997.

Tzanis A. and Vallianatos F.: A physical model of electrical earthquake precursors due to crack propagation and the motion of charged edge dislocations, in: *Seismo Electromagnetics (Lithosphere–Atmosphere–Ionosphere–Coupling)*, TerraPub, 2002, pp. 117–130, 2002.

Utada, H., Shimizu, H., Ogawa, T., Maeda, T., Furumura, T., Yamamoto, T., Yamazaki, N., Yoshitake, Y. and Nagamachi, S.: Geomagnetic field changes in response to the 2011 off the Pacific Coast of Tohoku earthquake and tsunami, *Earth Planet. Sci. Lett.*, 311, 11–27, doi:10.1016/j.epsl.2011.09.036, 2011.

Vallianatos, F. and Tzanis, A.: Electric Current Generation Associated with the Deformation Rate of a Solid: Preseismic and Coseismic Signals. *Phys. Chem. Earth*, Vol. 23, No. 9-10, pp. 933-938, 1998.

1 Vallianatos, F. and Tzanis, A.: On the nature, scaling and spectral properties of pre-seismic ULF signals.  
2 Natural Hazards and Earth System Sciences, 3: 237–242, European Geosciences Union, 2003.  
3

4 Vallianatos, F. and Triantis, D.: Scaling in Pressure Stimulated Currents related with rock fracture,  
5 Physica A, 387, 4940–4946, <https://doi.org/10.1016/j.physa.2008.03.028>, 2008.  
6

7 Venegas-Aravena, P., Cordaro, E. G., and Laroze, D.: A review and upgrade of the lithospheric dynamics  
8 in context of the seismo-electromagnetic theory, Nat. Hazards Earth Syst. Sci., 19, 1639–1651,  
9 <https://doi.org/10.5194/nhess-19-1639-2019>, 2019.  
10

11 Vigny, C., Socquet, A., Peyrat, S., Ruegg, J.-C., Metois, M., Madariaga, R., Morvan, S., Lancieri, M.,  
12 Lacassin, R., Campos, J., Carrizo, D., Bejar-Pizarro, M., Barrientos, S., Armijo, R., Aranda, C., Valderas-  
13 Bermejo, M.-C., Ortega, I., Bondoux, F., Baize, S., Lyon-Caen, H., Pavez, A., Vilotte, J.P., Bevis, M.,  
14 Brooks, B., Smalley, R., Parra, H., Baez, J.-C., Blanco, M., Cimbaro, S. and Kendrick, E.: The 2010 Mw  
15 8.8 Maule Megathrust Earthquake of Central Chile, monitored by GPS. Science 332, 1417–1421, 2011.  
16

17 Yue, H., Lay, T., Rivera, L., An, C., Vigny, C., Tong, X. and Báez Soto, J.C.: Localized fault slip to the  
18 trench in the 2010 Maule, Chile Mw = 8.8 earthquake from joint inversion of high-rate GPS, teleseismic  
19 body waves, InSAR, campaign GPS, and tsunami observations, J. Geophys. Res. Solid Earth, 119, 7786–  
20 7804, [doi:10.1002/2014JB011340](https://doi.org/10.1002/2014JB011340), 2014.  
21  
22

## Captions Figures

Figure 1: Schematic description of the non-constant uniaxial stresses in presence of a fault with friction coefficient  $\mu$  and dip angle  $\theta$ .

Figure 2: Dimensionless representation of normalized first and second temporal change of the uniaxial stress used by Venegas-Aravena et al. (2019). According to De Santis et al. (2019a) the earthquakes occur close to the center of figures. Here it is when  $t = t_0 = 10$ .

Figure 3: Temporal behavior of the semi brittle-plastic friction coefficient using different parameters. In all the cases it's possible to observe an increase in the friction before earthquake ( $t = 10$ ). However, the friction decrease after the earthquake only if  $k_2$  and  $k_4$  has values of  $\sim 10^{-9}$ .

Figure 4: Schematic description of friction gradient on the fault. When a constant and non-constant temporal stress change is applied at different paces within the lithosphere, a non-zero friction coefficient gradient is expected.

Figure 5: Total friction coefficient from the Seismo-electromagnetic Theory derivation. If we consider one point within the rupture area, the highest values of friction is found before the earthquake ( $t = 10$ ). The friction decrease at  $t=10$  was calculated using the stress drop in function of the co-seismic magnetic field. The maximum value is not completely recovery after the earthquake occur.

Figure 6: Schematic comparison among different friction behaviors related with seismic rupture area. Above the result of friction in the context of The Seismo-electromagnetic Theory is presented. At the bottom the classical view of the friction. When the rupture occur, de friction drop is observed in the two theories. However, exist a friction increase in the case studied in this work.

Figure 7: Spatial distribution of  $\gamma$  and  $\gamma_2$ . This functions represent the different sections (or behavior) of friction on the fault along x-direction. The distribution  $\gamma_2$  represent the stress drop section and distribution  $\gamma$  represent the semi brittle-plastic influence region.

Figure 8: Spatial-temporal Total Friction Coefficient  $\bar{\mu}_T(x, t)$  along fault x-direction using  $k_2 = k_4 = 10^{-9}$ , and the right color bar indicate the friction coefficient values at a certain time and position. The earthquake occur when  $t = 10$ . At this time, the stress drop (defined by the distribution  $\gamma_2$ )  $\Delta\tau \in [8,12]$ .

Figure 9: Same spatial-temporal Total Friction Coefficient, however, using  $k_2, k_4 = 10^{-10}$ .

Figure 10: Total Friction Coefficient using no semi brittle-plastic contribution. That is  $\gamma(x) = 0, \forall x \in [0, 2x_{half}]$ . The friction variation exist only when the earthquake occur ( $t = 10$ ) and at the earthquake rupture place ( $\Delta\tau \in [8,12]$  in this case).

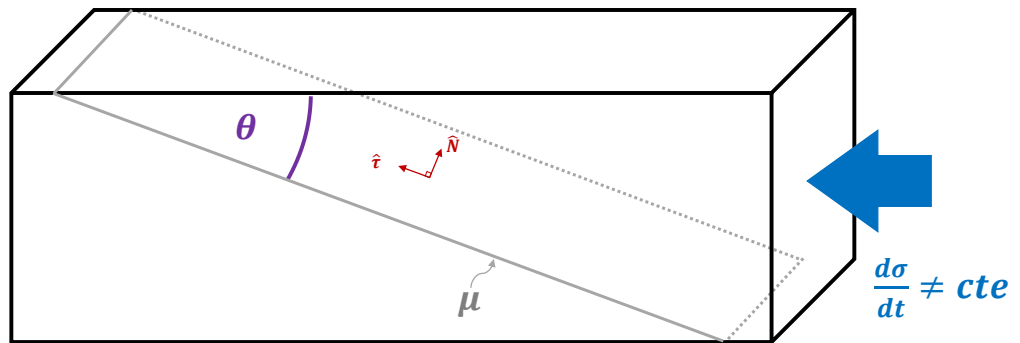
Figure 11: Above: The b-value using  $\sigma = \alpha \tau$ ;  $k_2 = k_4 = 10^{-9}$  and  $\alpha = 0.01$ . Bottom: The Gutenberg-Richter Law for instants time  $t = 0, t = 9$  and  $t = 20$ . The b-value decreases before the earthquake implying stronger seismic events.

Figure 12: The b-value and Gutenberg-Richter Law using  $k_2 = k_4 = 10^{-10}$ . The green and red curves are the same.

Figure 13: Different rupture's time viewed from the differential total friction coefficient  $d\bar{\mu}_T$  and using different values of  $k_2$  and  $k_4$ . The rupture occurs after the maximum differential total friction coefficient  $(d\bar{\mu}_T)_{MAX}$ , when  $d\bar{\mu}_T$  have values close to 0.5-0.9 times  $(d\bar{\mu}_T)_{MAX}$ .

1

Figure 1

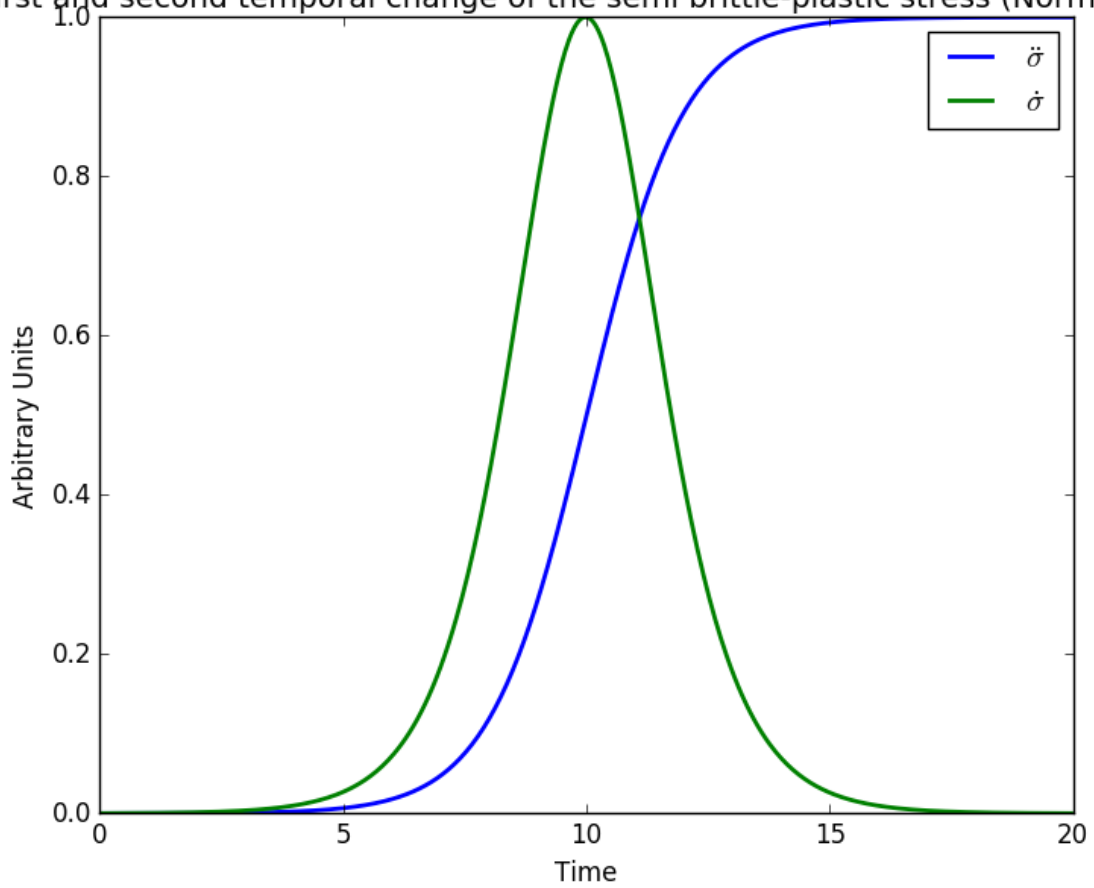


2

3

Figure 2

First and second temporal change of the semi brittle-plastic stress (Normalized)

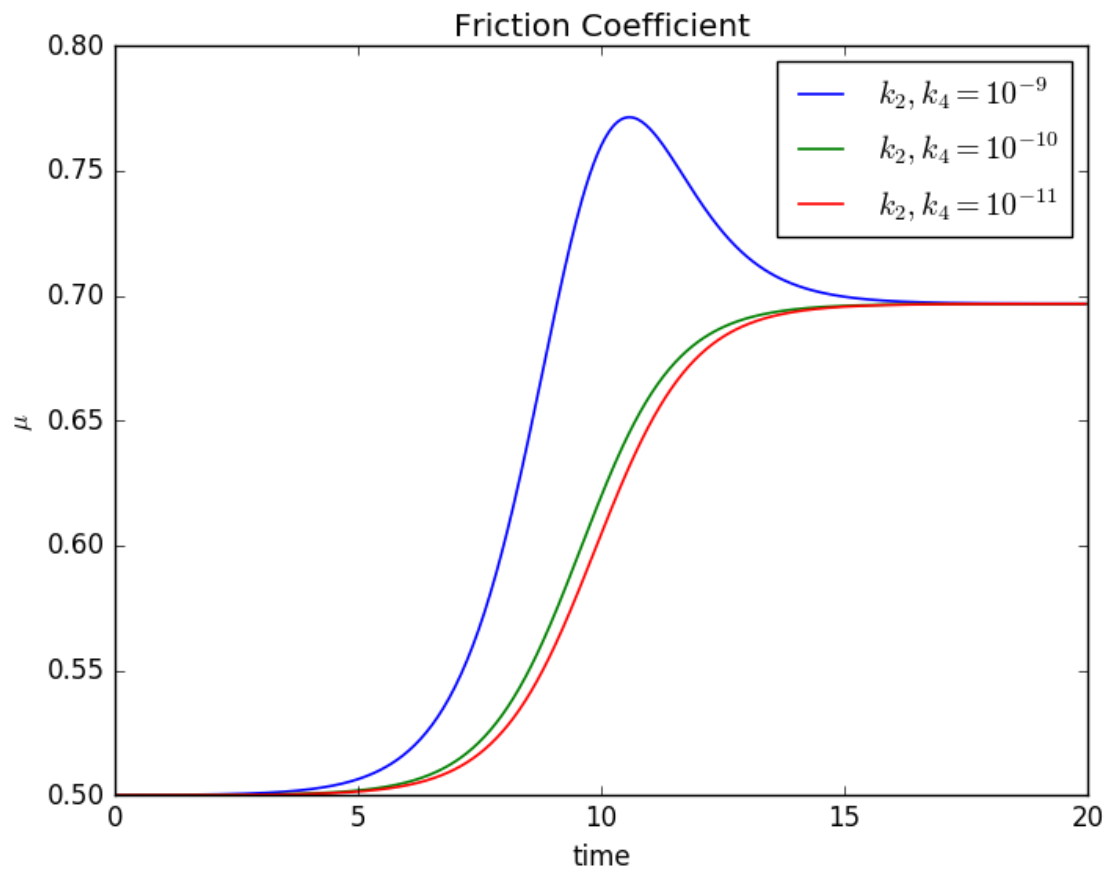


4

1

2

Figure 3



3

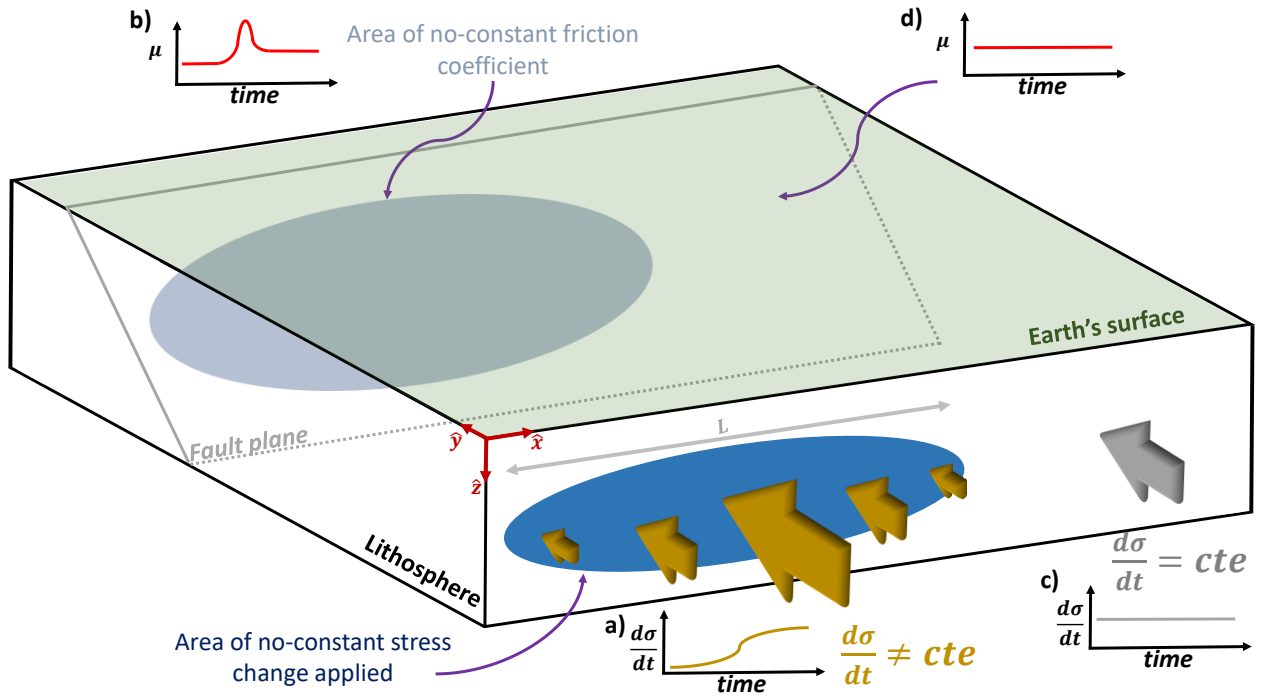
4

5

6

1

Figure 4



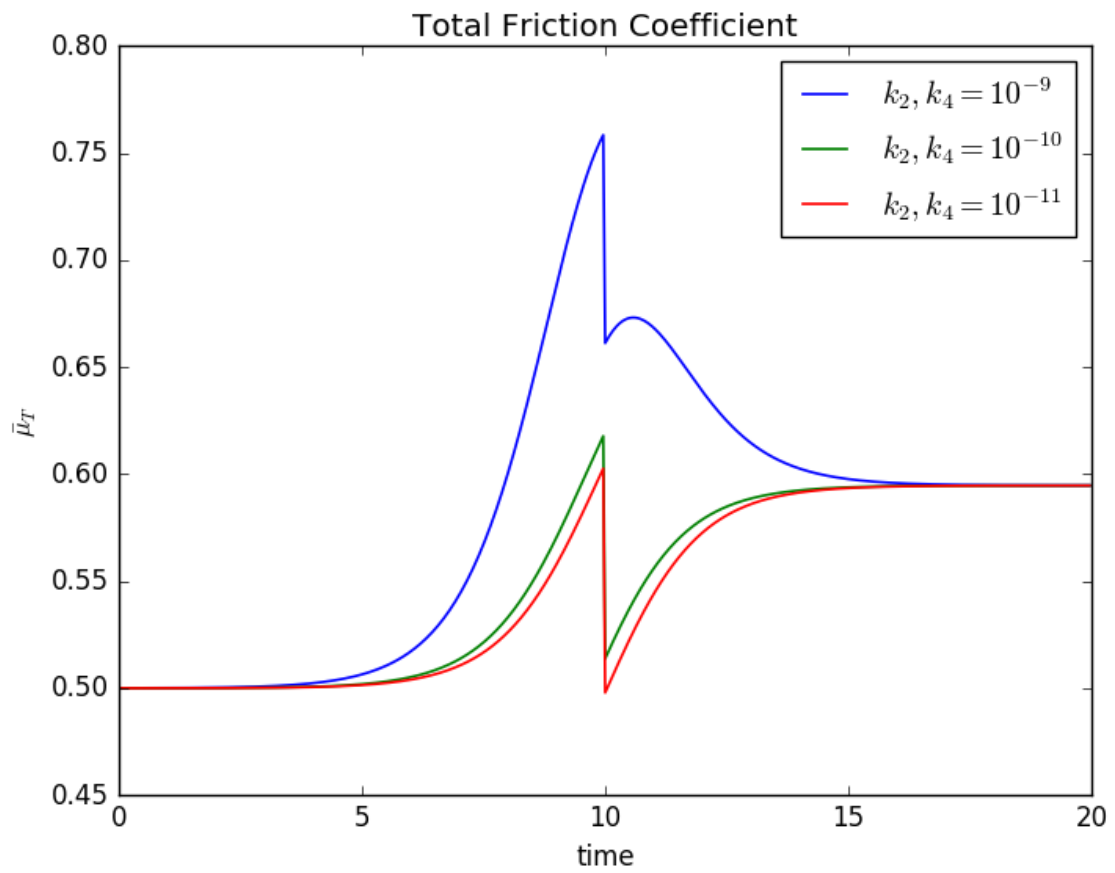
2

3

4

1

Figure 5



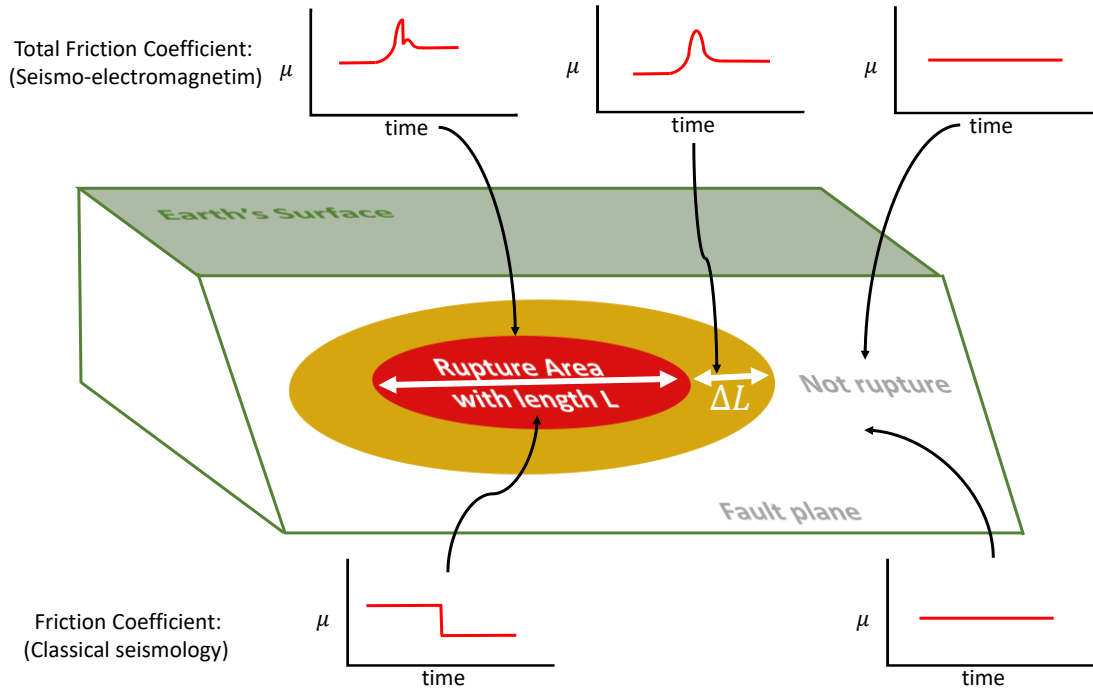
2

3

4

1

Figure 6



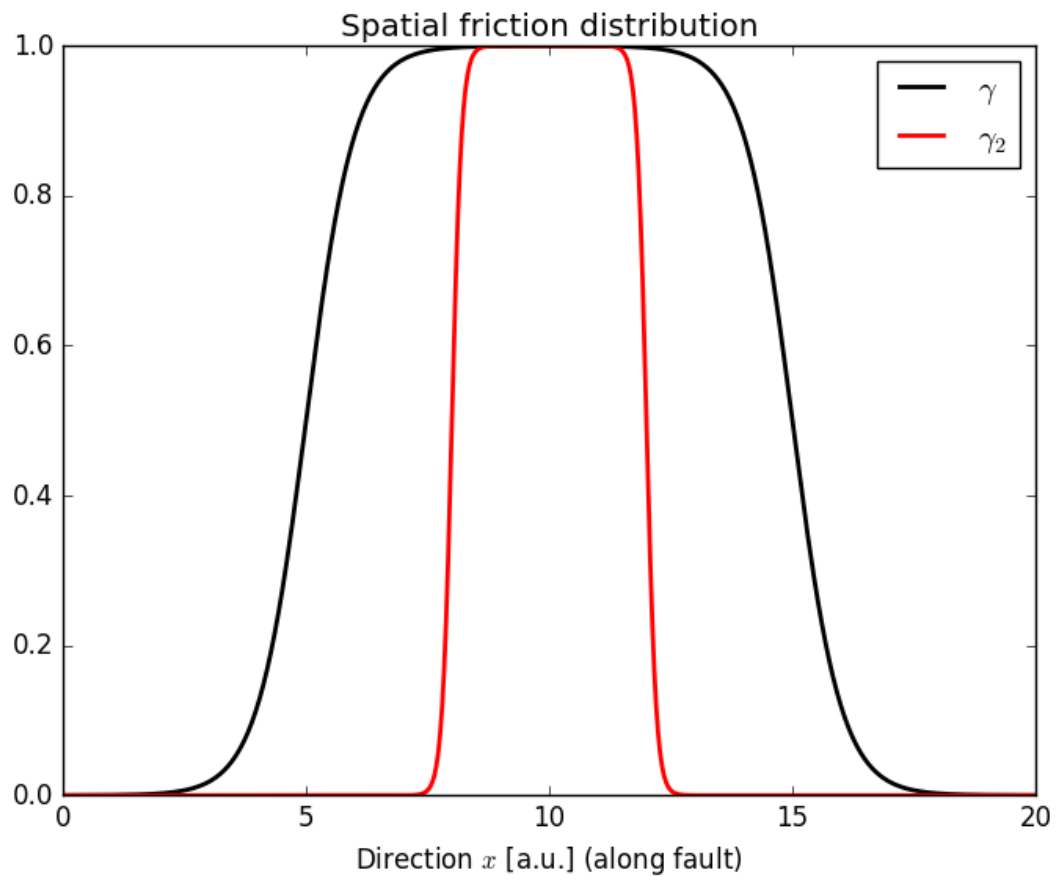
2

3

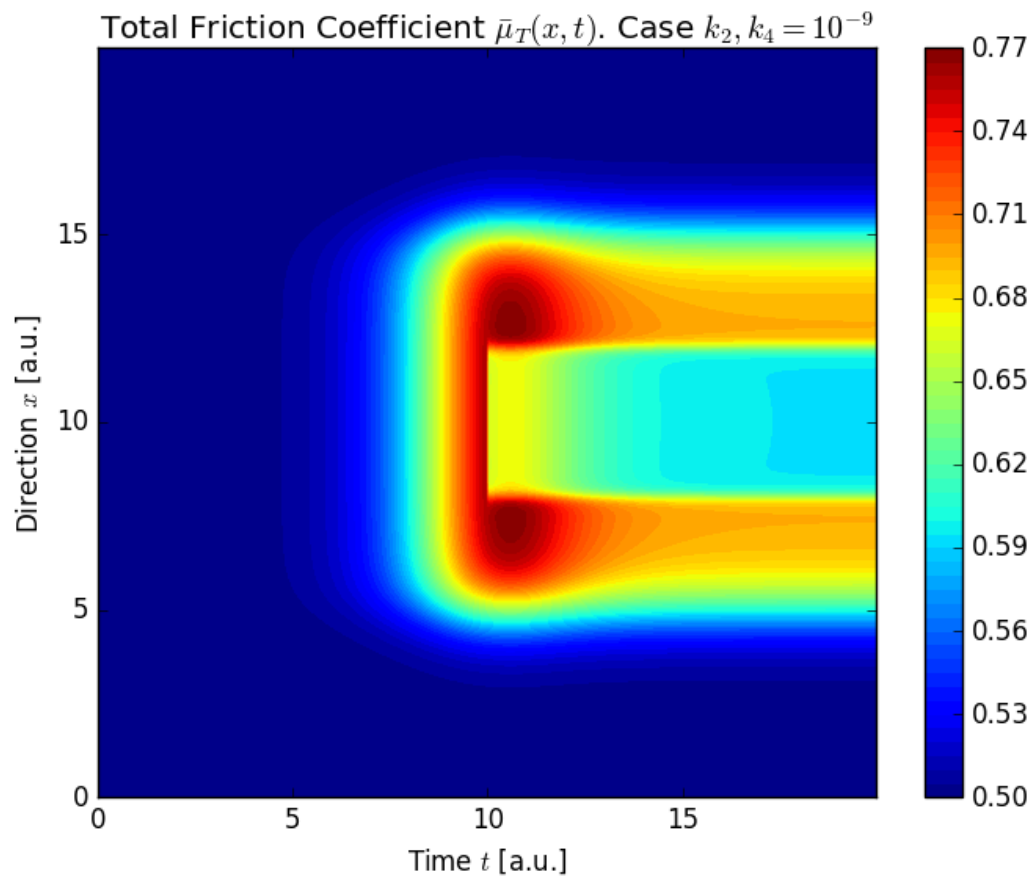
4

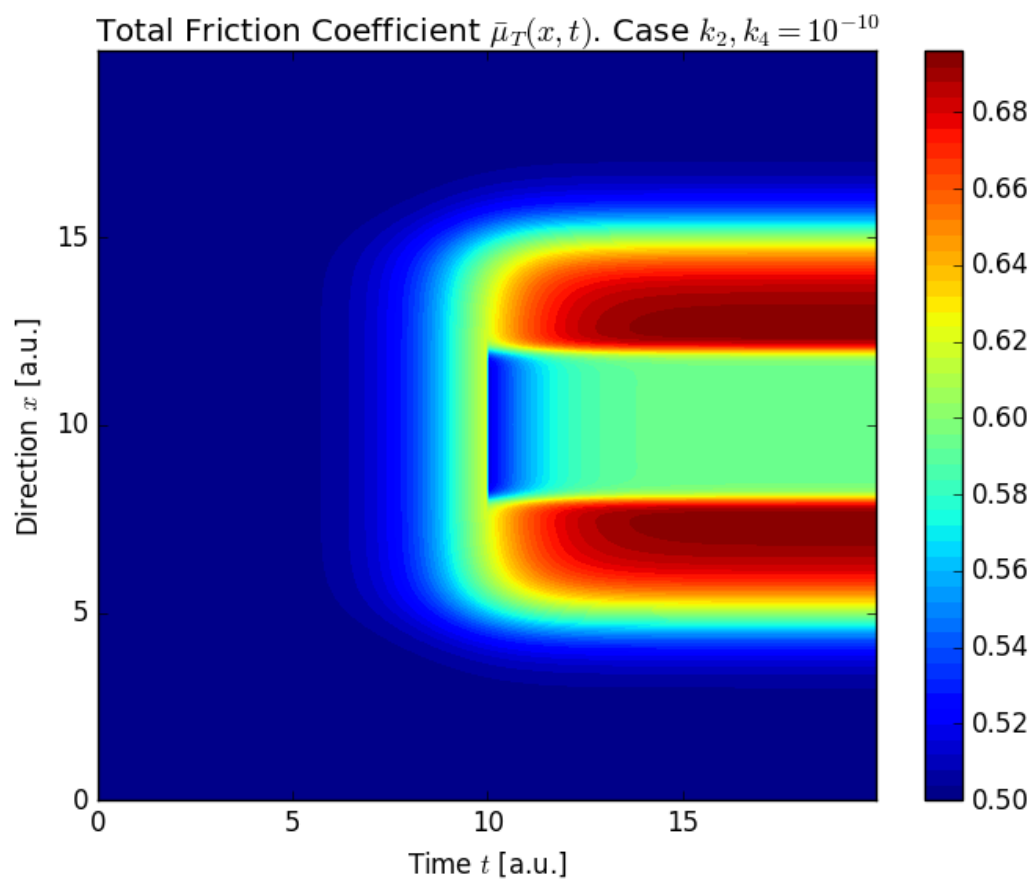
1

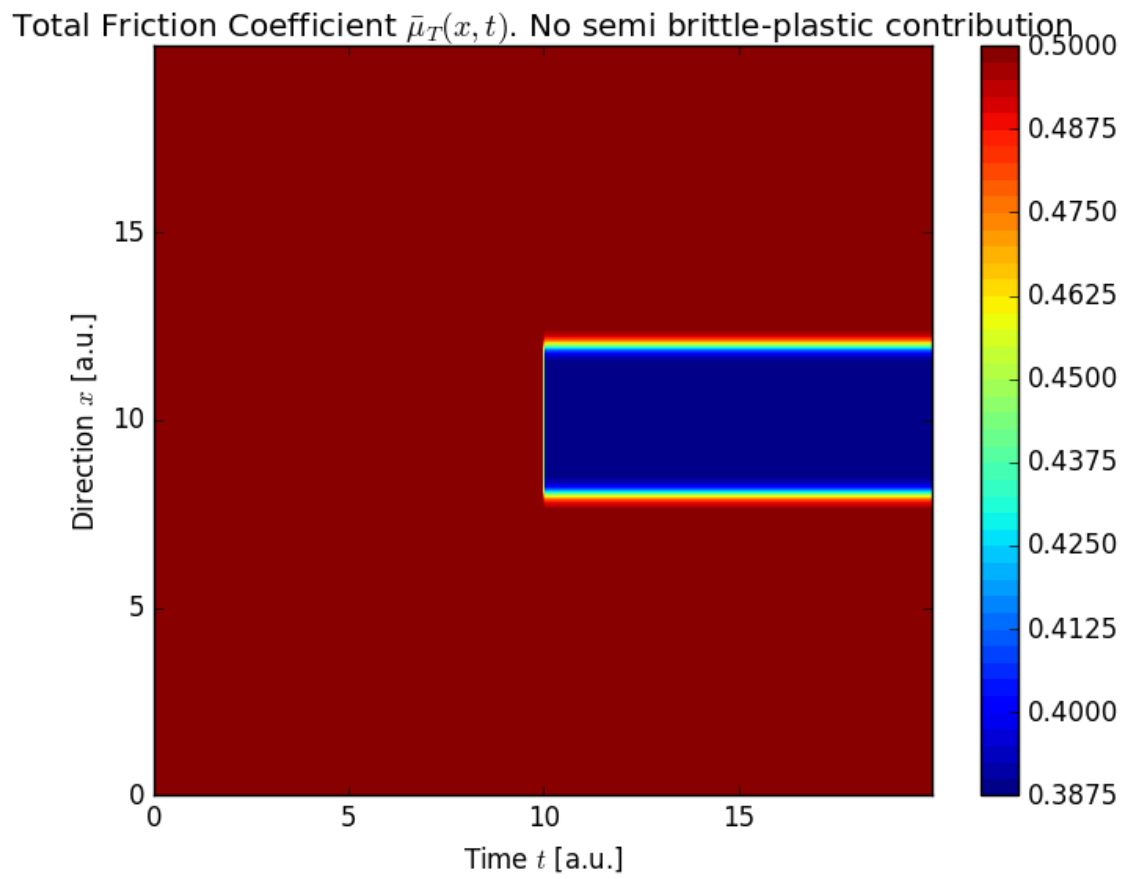
Figure 7



2

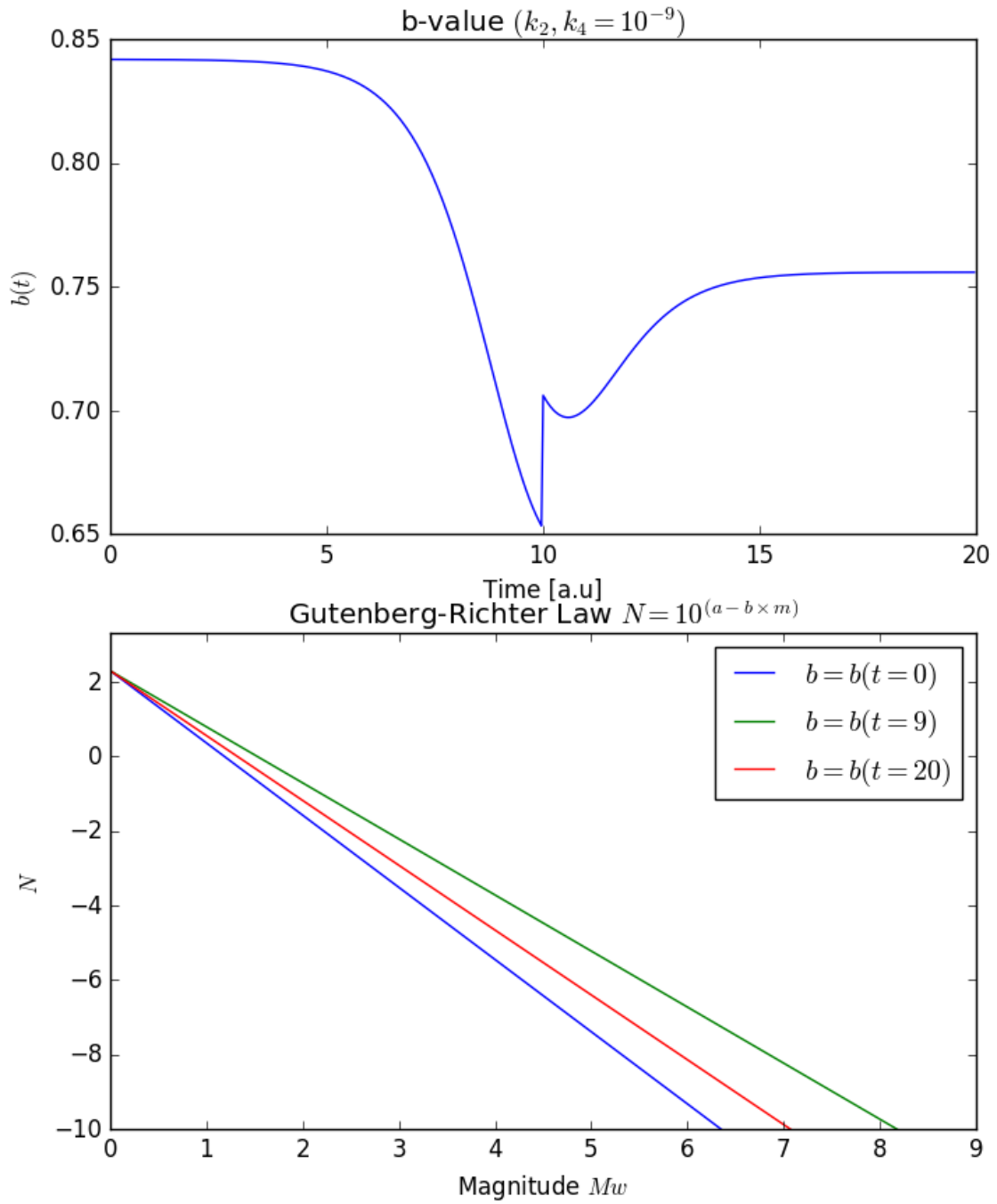






1

Figure 11

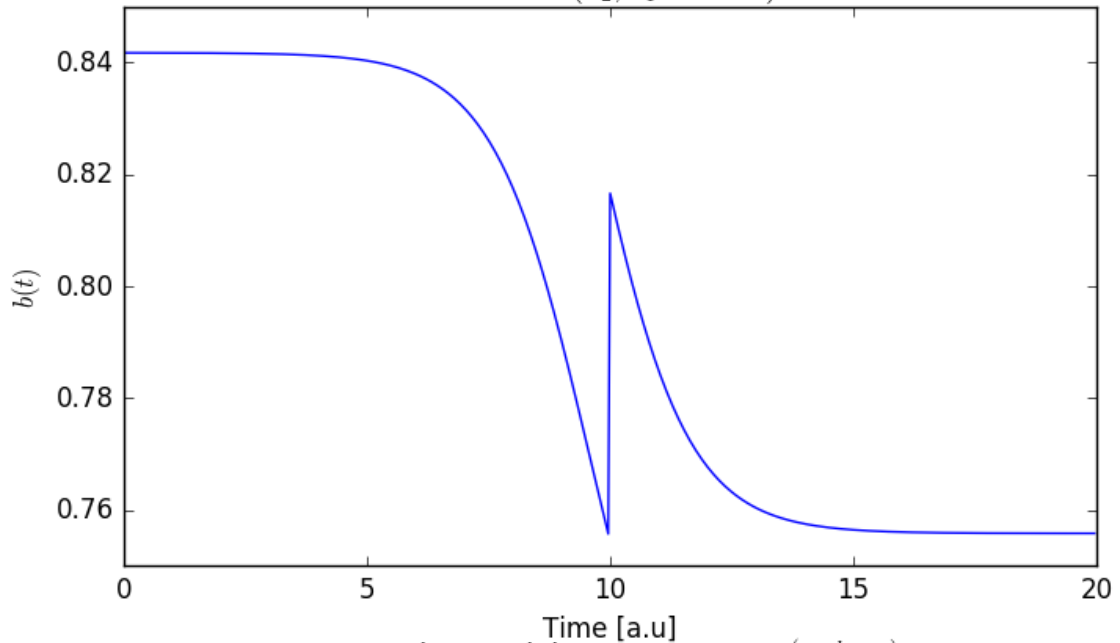


2

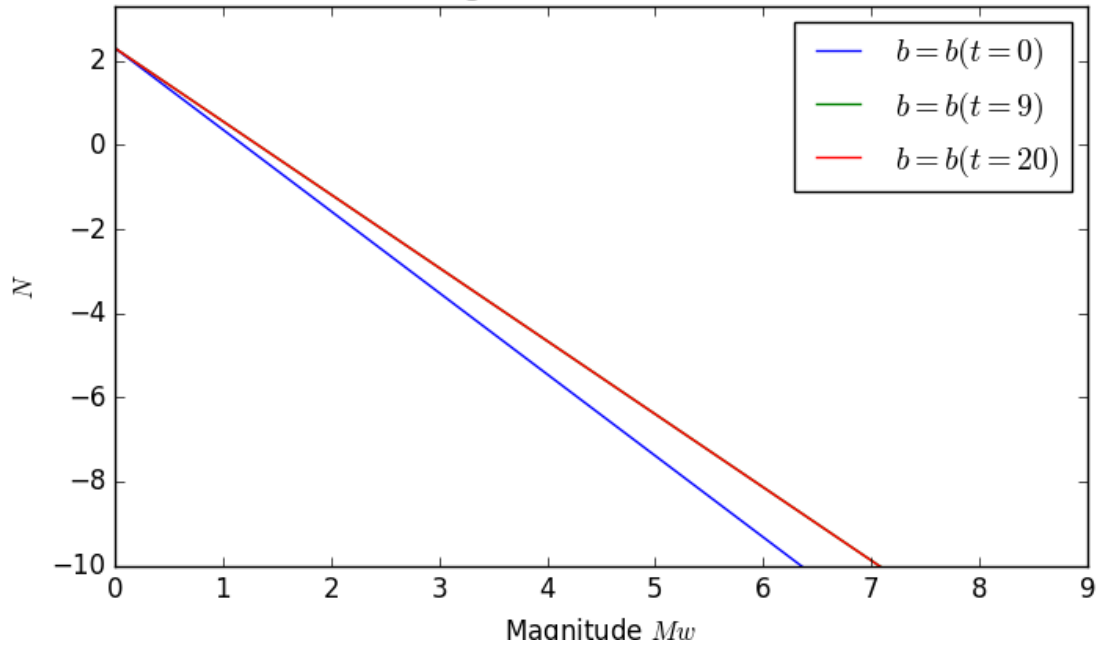
3

1

Figure 12  
b-value ( $k_2, k_4 = 10^{-10}$ )



Gutenberg-Richter Law  $N = 10^{(a-b \times m)}$



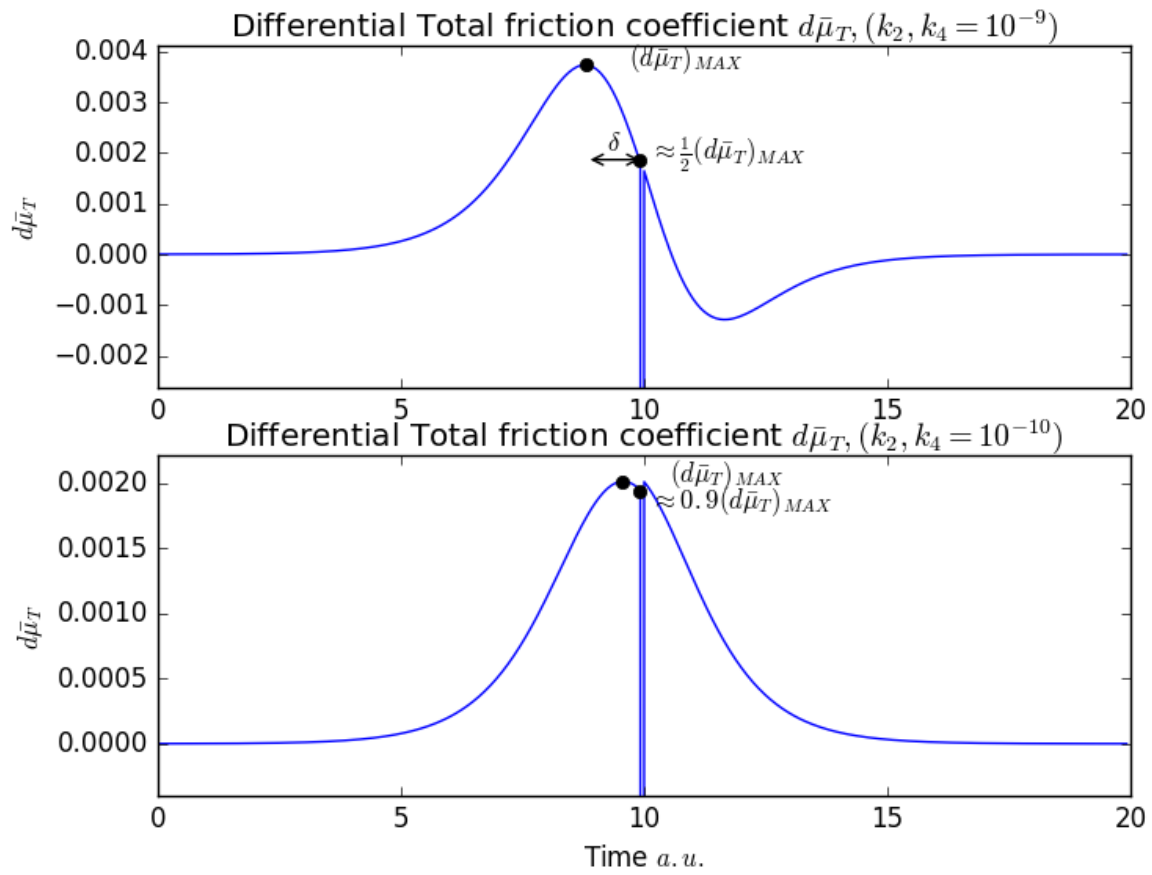
2

3

4

1

Figure 13



2